Liquid Jet-Array Cooling Modules for High Heat Fluxes

Chang H. Oh
Idaho National Engineering and Environmental Lab,, Lockheed Martin Idaho Technologies Company, Idaho Falls, ID 83415

John H. Lienhard V, Hesham F. Younis, Rudy S. Dahbura, and Dirk Michels
W. M. Rohsenow Heat and Mass Transfer Lab., Dept. of Mechanical Engineering, Massachusetts Institute of Technology, Cambridge, MA 02139

Liquid jet-array cooling modules had been designed for operation at very high heat fluxes and were used to remove fluxes as high as 17 MW/m^2. Experimental results, numerical studies, and thermal stress analyses are reported. Modules having actively cooled areas of 10 cm^2 were developed. Cooling is provided by an array of small-diameter water jets operating at speeds of 47 m/s. These jets impinge on the rear side of a 2- to 4-mm-thick metallic faceplate from which the heat load is absorbed. Cooling is entirely convective without boiling. The behavior of cooling jet arrays is summarized, including numerical simulations for our specific cases. Finite-element studies of the stresses in candidate faceplate materials are described for typical thermal and mechanical conditions. A thin-film high-flux resistance heater provides the heat load for testing module prototypes. The thermal resistances of the system are quantified experimentally and incorporated in our numerical model. The dominant thermal resistance is associated with the heating element. The modules are believed to be serviceable to fluxes above 20 MW/m^2, although difficulties with the heating element prevented this level from being reached.

Introduction

High heat flux systems may generally be separated into one of two categories: those requiring a moderately high heat flux over a large area, and those involving a hot spot with extremely large flux over a small area. Few designs are capable of removing an extremely large flux over a large area. Quantitatively, small areas may be regarded as those of a few square millimeters and extremely high fluxes may be regarded as those above 10 MW/m^2. While the precise demarcations are somewhat arbitrary, there is clearly a need for systems that support fluxes in the range of 10 MW/m^2 or more over areas of several square centimeters or more.

In this article, we report on efforts to support heat fluxes in the range of 10 MW/m^2 over areas of 10 cm^2. We have designed cooling modules that use an array of impinging liquid jets to convectively cool the rear of a faceplate, whose forward surface is subject to an imposed heat load. The source of this load is arbitrary, but potential applications include plasmas and optical beams that interact with the front surface of the faceplate. With minor alterations in the design, the faceplate itself could be the source of the heat load, as might occur if it were a microwave component or a semiconductor-laser array.

Impinging liquid jets have been demonstrated to be an effective means of establishing high heat-transfer rates in industrial transport processes (Sun et al., 1993; Viskanta, 1993; Ma and Bergles, 1988). A turbulent jet impinging orthogonally onto a plane surface produces, in the vicinity of the stagnation point, some of the highest heat-transfer coefficients encountered in single-phase convection (Cooper et al., 1993; Craft et al,, 1993). This performance is due to the thin hydrodynamic and thermal boundary layers formed in this region by the jet deceleration.

The stagnation pressure of a high-speed liquid jet significantly raises the saturation temperature and can enable high wall temperatures and correspondingly high heat fluxes to exist in the stagnation zone (Liu and Lienhard, 1993). Both the pressure and the heat-transfer coefficient drop rapidly as the distance from the stagnation point increases. Consequently,

individual jets are unsuitable for high-flux cooling of areas significantly larger than the cross-sectional area of the jet, Our approach is to place an array of jets on a tightly spaced hexagonal platform (3 to 4 jet diameters center to center) so as to limit the area cooled by each jet to diameters of only 3 to 4 times the jet diameter. Such arrays can largely compensate for the radial decrease in the heat-transfer coefficient (Pan and Webb, 1995), and can slightly compensate for the declining pressure. This arrangement will not sustain fluxes as high as may be reached within the stagnation zone of a single jet, but should support fluxes within our range of interest.

The other significant barrier to high flux cooling over large surfaces is the mechanical failure of the heat-transfer surface -in this case, the module's faceplate. These surfaces must have a thickness of a few millimeters at most in order to limit heat conduction resistance, yet they must withstand temperature differences of several hundred degrees Celsius across their thickness. Consequently, thermal stresses are large while the hot spot surface is at a temperature that may soften the faceplate material. Moreover, pressure loads from the cooling system can be significant. The heat-transfer surface must be designed to survive these conditions, which requires careful consideration of the stresses in surface and identification of materials with appropriate thermal and elastic properties.

For testing purposes, we have also needed to devise an appropriate electrical resistance heater, producing fluxes up to 40 MW/m^2. The heater must mate with the faceplate without introducing a large thermal resistance or undesired mechanical loads. We have used thermally-sprayed metal films for this purpose.

Numerous numerical investigations of impinging axial and radial jets were performed by Owsenek et al. (1997) and Meyer (1994). These studies, however, are based on a single jet impinging orthogonally onto a large plane surface, with much lower Reynolds numbers (a maximum of 70,000). Cooper et al. (1993) also investigated numerous turbulence models using various Reynolds numbers (23,000 and 70,000) and nozzle-to-diameter ratios. Our study is based on higher Reynolds numbers (up to 200,000) and multiple jets in a confined module that generate secondary stagnation zones when adjacent jets collide and exit along the symmetry line. We performed new numerical calculations is to evaluate the pressure and velocity distributions in the liquid and, in particular, to examine the effect of the nozzle position on the heat-transfer coefficient.

Cooling by Impinging Jets

Past work with free surface circular liquid jets (Liu and Lienhard, 1993) has shown that jets operating in the range of 100 m/s can carry fluxes as high as 400 MW/m^2. High velocity liquid jets produce thin boundary layers on the impingement surface and as a result very high heat-transfer coefficients can be attained. Extrapolation of existing correlations (Lienhard, 1995) into our range of Reynolds number (up to 200,000) predicts heat-transfer coefficients on the order of 200,000 $W/m^2 \cdot K$. These results have made the use of impinging liquid jets attractive in our application, provided we can suppress boiling burnout and provided the faceplate survives the mechanical and thermal stresses. If sufficient liquid pressure can be maintained, boiling can be avoided and critical heat flux limitations (Katto and Shimizu, 1979) to heat-transfer rates will not be an obstacle. For the pressure used in this study, boiling is not expected until fluxes in excess of 20 MW/m^2.

Free surface jets

Previous work on single free surface jets has shown the stagnation zone of an impingement jet to be in the range $0 < r/d < 0.8$, where r is the radial distance along the wall from the stagnation point and d is the jet diameter (Liu et al., 1991). It has been experimentally verified that this region is of a nearly constant Nusselt number. Beyond the stagnation zone, the heat-transfer coefficient drops rapidly with radius as a result of growth of the boundary layer and the flow's deceleration along the wall. Consequently, the heat-transfer coefficient drops by about 50% from the stagnation zone value at a radius of $4d$ to $6d$. Pressure also drops with distance from the stagnation point in a Gaussian manner. Liu et al. (1993) analytically obtained pressure distributions of laminar liquid jets including surface tension effects. For an infinite Weber number, the pressure drops to 70% of its stagnation point value at $r/d = 0.75$. The stagnation point pressure is equal to

$$P_{stag} = P_{ambient} + \frac{1}{2}\rho u_j^2 \tag{1}$$

for u_j the jet speed and ρ the liquid density. Thus, a 50 m/s water jet has a stagnation point pressure of 1.34 MPa (193 psia), which drops to 400 kPa (58 psia) at $r/d = 0.7$ and to the ambient pressure beyond $r/d = 1$.

Submerged jets

In the present system, the jets are enclosed in a manifold that contains no air and are therefore submerged. Submerged jets have a significantly different behavior from free surface jets for outside the stagnation zone, However, if the target is kept within the potential core of the jet (nozzles within a few jet diameters of the faceplate), the stagnation zones of both types of jet are identical (Lienhard, 1995). This is due to the fact that at such a spacing the core of the jet has not begun to mix with the surrounding fluid.

In submerged water jets, it has been observed that stagnation Nusselt numbers increase to a maximum (Sun et al., 1993) at $z/d = 5$ to 6. This has been attributed to an increase in turbulence levels with increasing nozzle- to- plate separations owing to the increased mixing of the jet with its surroundings. Beyond $z/d = 5$, the Nusselt numbers drop monotonically from their peak. The increased mixing comes at the expense of a decreased mean speed of the jet. Larger standoff distances allow more drag by surrounding liquid on the jet, while smaller distances allow for higher fluid momentum on the impinging wall and keep the downstream wall boundary layers thinner. Nozzle-to-target spacing tighter than $z/d = 1$ raises the flow resistance and the required supply pressure without producing a significant improvement in h; for thick walled tubes, in particular, a tight spacing can lower the stagnation zone h.

Because of similarity in stagnation zones, it is reasonable to assume that the pressure distributions and Nusselt numbers will be similar to those of free surface jets in the stagnation region when z/d is not large. Sun et al. have performed experiments to analyze the stagnation Nusselt number range $5{,}000 < \mathrm{Re} < 36{,}000$. Their stagnation zone Nusselt numbers generally agree very well with Steven and Webb's (1991) data for free surface jets.

Jet arrays

The reduced cooling performance outside the stagnation zone of a single jet poses a problem in high heat flux systems, since pressures and heat-transfer coefficients drop rapidly. To eliminate some of the shortcomings of jets in cooling at large distances from the stagnation point, our cooling modules use an array of closely spaced jets. The faceplate is effectively divided into sub-regions associated with each individual jet, within which the heat-transfer coefficient remains closer to the stagnation zone value. Fewer data are available for arrays of liquid jets, particularly at high Re_d. The hydrodynamics between the various jets differ considerably from the conditions for single jet cooling. In particular, the liquid from adjacent jets collides along the lines of symmetry between nozzles, creating secondary stagnation zones on the wall; for example, the secondary stagnation zone will form a hexagon surrounding the central jet in our array. Within these secondary stagnation zones, momentum conservation requires the pressure to rise significantly above the ambient pressure as the liquid turns 90° and moves normally away from the wall; in addition, h has also been observed to rise in experimental studies.

The specific variations of h with radial distance from the stagnation point depend on the Reynolds number, nozzle-to-nozzle spacing, and array platform; however, existing data (Pan and Webb, 1995) for similar. configurations at lower Reynolds numbers than ours show a minimum h of about 75% of the stagnation value at a radius of about d and a secondary peak of about 90% of the stagnation value in the secondary stagnation zone (radius of 1.8 d for our array spacing). Our Reynolds numbers are ten times higher than the upper limit of Pan and Webb's experiments; nonetheless, the result provides some guidance as to what fraction of the stagnation point the heat-transfer coefficient will be achieved as an average beneath the jet array.

Liquid pressures will be maximum in the stagnation zone, will drop to a minimum at larger radii, and will rise slightly at the secondary stagnation zone. The minimum pressure region is the most likely location for boiling to begin. We apply a back pressure to the module to keep the saturation temperature in this region high.

Experimental Apparatus

Cooling module

The cooling modules are integral heat-sinking units that can be incorporated into an end-user's system for the removal of large fluxes. As shown in Figures 1 and 2, these modules are comprised of a flat plate that absorbs the principal heat load, an underlying array of pressurized high velocity liquid jets, and a liquid manifolding arrangement. The liquid can be either water or another suitable fluid, depending on specific application requirements.

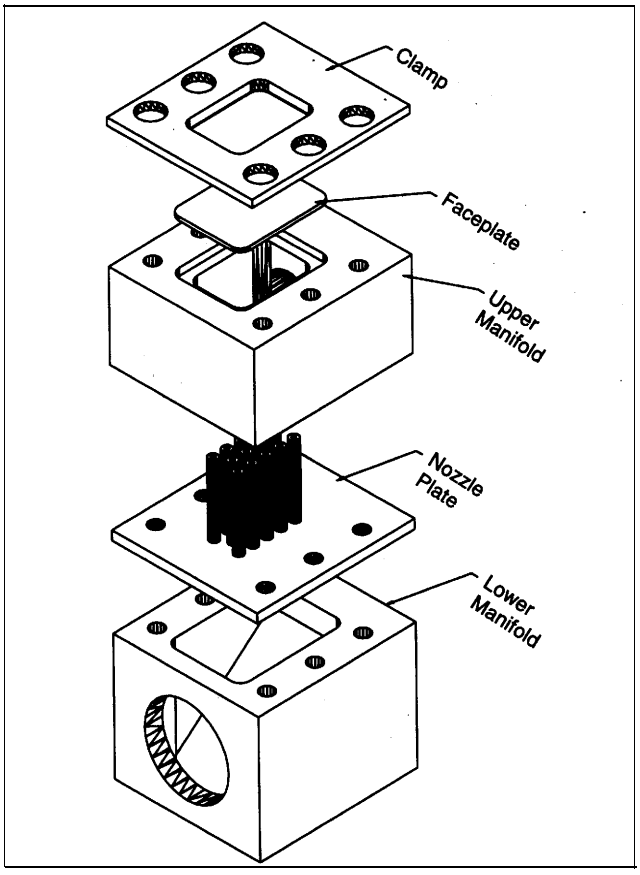

Figure 1. Cooling module configuration.

A hexagonal array of 14 water jets was designed for operation of heat fluxes of up to 40 MW/m^2 with jet velocities of up to 52 m/s (Lienhard et al., 1996). The lower manifold is at a higher-pressure than the upper manifold and is tapered to limit streamwise variations in dynamic pressure. The liquid is driven into the tube nozzles from the higher-pressure manifold to the lower-pressure manifold. Bleeder valves allow air to be purged from both manifolds. The nozzles have an inner

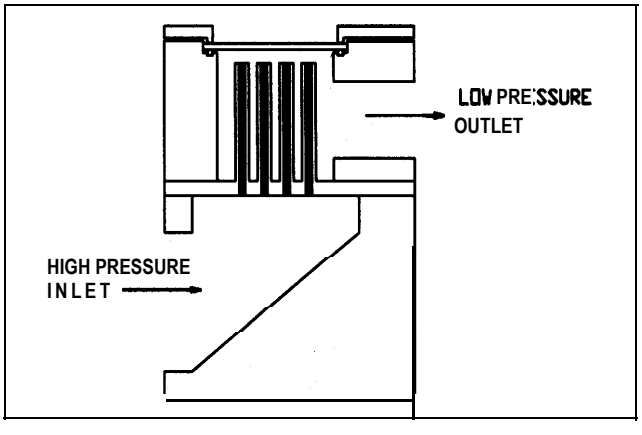

Figure 2. Module cross-section illustrating the flow path.

diameter $d = 2.78$ mm and are spaced 10 mm center to center. The nozzles have an outer diameter of 6.35 mm and are 5.0 cm in length. The nozzle inlets are contoured to reduce head loss. The liquid experiences a pressure drop across the nozzles and a rise in velocity u_j related by

$$\Delta P_{\text{nozzles}} \cong 1.47\left(\frac{1}{2}\rho u_j^2\right) \tag{2}$$

which is obtained from direct measurements and is in good agreement with an analytical pressure drop calculation. Thus, by controlling A P_{nozzles} using the valve at the test section outlet, the flow rate through the nozzles can be varied. The liquid impinges onto the faceplate. The Reynolds numbers $Re_d = (u_j d)/\nu$ are in the range of 100,000 to 200,000 depending on the jet speed and the property reference state at which the kinematic viscosity ν is evaluated.

In all experiments reported here, the upper manifold was set to a backpressure of 580 kPa, corresponding to a saturation temperature of 157°C and a jet velocity of 46.5 m/s at the nozzle outlets. The nozzle outlets are located 5.6 mm below the faceplate ($z/d = 2$).

The faceplates (5.1 by 6.6 cm) are made from either a dispersed-strengthened copper alloy (C15715) or a molybdenum alloy TZM. The faceplate sits in a groove machined into the upper manifold, with a silicone O-ring beneath it and a clamping frame above it to secure it to the upper manifold, This clamp is designed to allow lateral expansion that relieves thermal membrane stresses. Alloy Cl5715 contains 0.3% aluminum oxide and has a thermal conductivity of approximately 365 M/m K at 20°C. The TZM alloy is a powder metal product and contains 0.5% Ti and 0.08% Zr with a thermal conductivity of approximately 120 W/m K at 20°C. Both alloys have been found to be excellent materials for high heat flux surfaces (Lienhard and Napolitano, 1998). Flow through the cooling module, with no heating, results in a slight temperature increase due to viscous dissipation. A first law balance for the cooling module yields the following relationship for the viscous temperature rise as a function of the cooling module pressure loss

$$\Delta T_{\text{bulk}} = \frac{\Delta P \cdot \dot{Q}}{\dot{m} \cdot C_p} = \frac{\Delta P}{\rho C_p} \tag{3}$$

This result is in good agreement with the average measured temperature rise of $\Delta T_{\text{bulk}} = 0.4$°C without heating. With heating, the bulk temperature rise may reach 1.5°C.

Flow loop components

The flow loop is shown in Figure 3. The flow loop consists of a water reservoir, turbine flowmeter, pump, cooling module, valves, and pressure transducers. Water flows from a 500-gal (1,900 L) capacity reservoir at low pressure through a 2-in., (51-mm) pipe where the flow rate is recorded by a turbine flowmeter. The pipe diameter is then increased to 2.5 in. (64-mm) to match the pump entrance. The pump is an eight stage centrifugal pump driven by a 30 hp motor, and is rated at 2 MPa (300 psi) and 6.31 L/s (100 gpm). After experiencing a pressure rise, the flow passes through 2.5-in. (64-mm) stainless steel piping, which is subsequently reduced back to 2 in, (51-mm). After the pressure drop in the test section, the flow returns to a low pressure and is guided back to the water reservoir. The pressure at the test section outlet is regulated with a 1.5-in. (38-mm) globe valve.

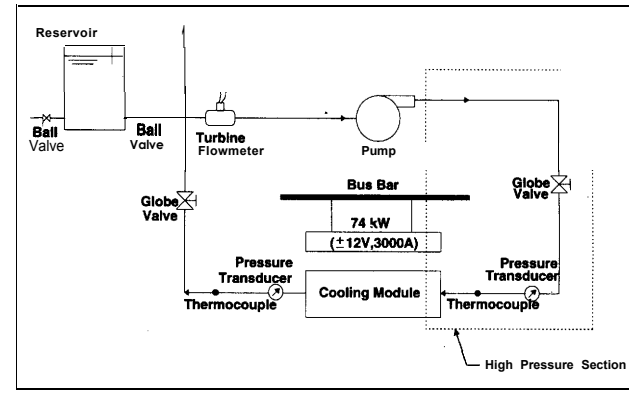

Figure 3. Flow loop.

The flow loop instrumentation includes a turbine flowmeter (accurate to ± 1%) with a digital rate meter and two diaphragm pressure transducers (accurate to ± 0.1%) with digital process meters. High-current DC power was delivered by bus bars to drive the heating element on the faceplate of the cooling module. Type K thermocouples (resolution of ±0.1°C) are fitted into the pipes on either side of the module, downstream of the pressure transducers.

Metal Film Resistance Heaters

The electrical resistance heaters consist of a thermally-sprayed metal film atop a thermally-sprayed ceramic insulating layer that is deposited onto the dry surface of the faceplate (see Figure 4). The heater/faceplate assembly consists of the metal faceplate (5.1 by 6.6 cm), an electrically insulating ceramic film (5.1 by 6.6 cm), and a metallic thin-film heater (3.3 by 5.1 cm). The ceramic fihn lies between the faceplate

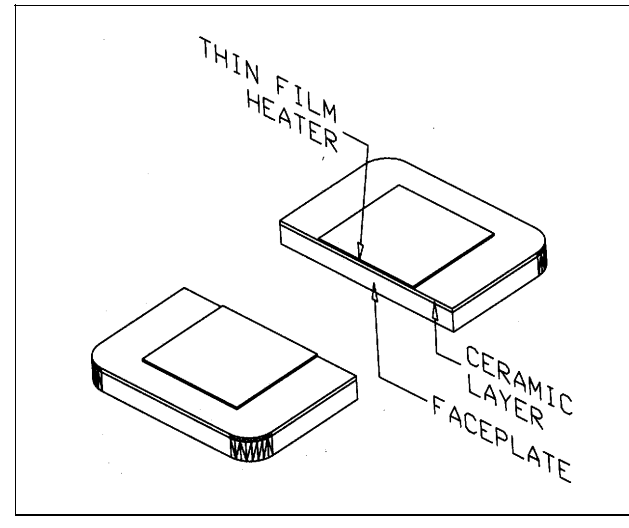

Figure 4. Thin film heater and insulating ceramic layer on the faceplate.

and the heater film. The films are located on the dry side of the faceplate, rather than the liquid side, because in applications heat flux will be applied to the dry surface of the cooling module. Details of the design of these heaters are given by Younis et al. (1997) and by Michels et al. (1998).

Electrical bus bars sit on the long edges of the metal film. The bars are each 6.3 mm wide, so that the actively heated region of the metal film has dimensions of 2.0 by 5.1 cm. A kinematically balanced mounting was designed to press the bus bars against the edges of the heater fihn. This mechanism allows lateral motion of the bus bars to ensure an even distribution of force over the contact surfaces. The magnitude of the contact area and uniformity of contact between the bus bars and the heater were verified using a pressure sensitive film. Electrical contact resistance at the joint between the bus bars and the heater was minimized by coating the joint with silver paint and was verified to be negligible.

Ideal materials for the thin film heaters are metals that combine a high melting point with high thermal conductivity and high electrical resistivity. The underlying electrically insulating layer should have a high thermal conductivity and should be only as thick as in necessary to provide adequate electrical isolation, so as to minimize its thermal resistance. The maximum attainable heat flux may be severely limited if the temperature rise across the thin films is too large, owing to the effects of temperature on material properties and large thermal expansion stresses.

In thermal spraying, high velocity particles impinge on the surface of the substrate and form splats. Velocity, size, and temperature of the particles strongly affect the size, spreading, and cooling of these splats, which in turn affect the deposit microstructure and material properties (Sampath and Herman, 1996). Different spray processes produce films of a different quality. In air plasma spraying (APS), significant porosity may be present in the deposited material. This leads to a much higher electrical resistivity and much lower thermal conductivity than for the bulk material. In vacuum plasma spraying (VPS), properties are close to those of the bulk material. In high-velocity oxygen fuel spraying (HVOF), properties are better than APS, but not quite as good as VPS. We have tested films made by each technique.

The films produced can vary in thickness by as much as $\pm 25\ \mu m$. Consequently, film nonuniformities that localize the resistive heating and produce variations in temperature are quite significant for thinner films. These temperature variations amounted to $\pm 70°C$ in a 76 μm thick APS molybdenum heater film, but only to $\pm 15°C$ in a 254 μm APS molybdenum heater film, both at an average surface temperature of 300°C. Variations are substantially lower (at a given thickness) for VPS films. Details of these variations are given by Younis et al. (1997) and Michels et al. (1998).

Table 1 summarizes some of the APS heater/faceplate configurations that were tested. Table 2 summarizes the VPS and HVOF configurations.

Thermal and Mechanical Faceplate Stresses

The stresses occurring in the faceplate are a function of temperature differences, heater geometry, liquid jet pressure loads, mechanical boundary loads at the faceplate edges, and material properties. An important parameter governing the maximum faceplate temperature is its thickness. In order to minimize the temperatures, the optimal faceplate design would use the minimum thickness required to withstand the force of the impinging liquid jets. Finite-element modeling (FEM) using the COSMOS/M package (1995) has been utilized as a design tool for the stress analysis.

Table 1. APS Heater/Faceplate Configurations Tested

Set	Heater Film	Insulation Film	Faceplate
A	Ni, 50 μm	MgO, 254 μm	C15715, 3 mm
B	Ni, 152 μm	Al_2O_3, 254 μm	C15715, 3 mm
C	Mo,254 μm	Al_2O_3, 203 μm	C15715, 3 mm
D	Mo,254 μm	Al_2O_3, 203 μm	TZM, 3.2 mm
E	Mo, 76 μm	Al_2O_3, 203 μm	TZM, 2.3 mm
F	Mo, 127 μm	Al_2O_3, 203 μm	TZM, 2.3 mm
G	Mo, 178 μm	Al_2O_3, 203 μm	TZM, 2.3 mm

Mechanical boundary conditions were used to simulate the pressure from the impinging liquid jets and the restraint at the edges of the plate. The pressure distribution resulting from the liquid jets has been modeled using a series of Gaussian surfaces given by

$$P(x,y) = P_{stag} \sum_{i=1}^{9} e^{-(x-X_i)^2/2\sigma^2} e^{-(y-Y_i)^2/2\sigma^2} \qquad (4)$$

The center of each surface (X_i, Y_i) is located at the stagnation point of an individual jet. A stagnation pressure P_{stag} of 1.24 MPa (180 psi), corresponding to a jet velocity of 50 m/s, was utilized. As the distance from the jet center increases, the pressure decreases. Due to the geometrical symmetry of the plate and the loading, a one-quarter plate model was utilized as a means to increase the number of FEM nodes per unit area of the plate. A total of nine jets were used in the one-quarter model. Only five jet centers lie directly within the quarter plate model. The remaining four are centered outside the quarter plate boundary.

The edges of the faceplate were modeled as simply supported; displacement normal to the face-plate was restricted at the edges while displacements in the plane of the plate were unrestricted. Rotational boundary conditions could not be applied, as the solid elements supported only 3 degrees of translational freedom.

The temperature of the faceplate depends on the applied heat load, the convective cooling, the faceplate material, and thickness. These simulations do not include the thermal resistance of the heater films. The faceplate temperatures increased with increasing thickness and heat flux. Due to their superior thermal conductivity, DS copper ($k \sim 350$ W/m·K) faceplates remained cooler than TZM ($k \sim 115$ W/m K)

Table 2. Configurations Tested Using HVOF Insulators with VPS or HVOF Heater Films

	Set	Heater Film	Insulating Film	Faceplate
VPS/HVOF	A	NiCr, 75 μm	Al_2O_3, 100 μm	C15715, 3.2 mm
	B	NiCr, 150 μm	"	C15715, 2.5 mm
HVOF/HVOF	C	NiCr, 280 μm	Al_2O_3, 100 μm	C15715, 4.0 mm
	D	NiCr, 100 μm	"	"
	E	NiCr, 125 μm	"	"

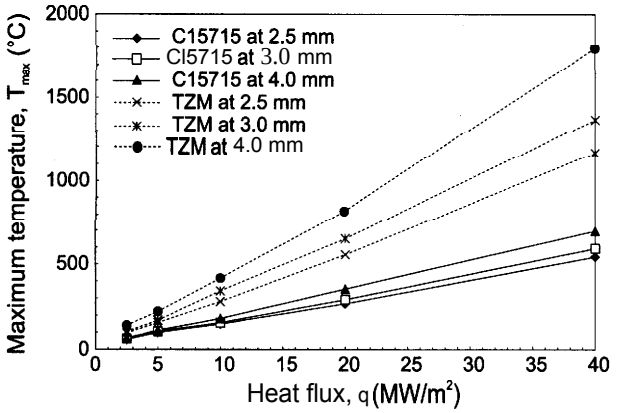

Figure 5. Maximum faceplate temperature as a function of the heat flux without heater films.

faceplates. At a heat flux of 2.5 MW/m^2, a 2.5 mm DS copper faceplate exhibited temperature changes up to 33% lower than the equivalent TZM faceplate. Figure 5 shows the maximum faceplate temperature, occurring on the heated surface at the plate center, as a function of the heat flux.

Two distinct zones of high stress occurred on the faceplate. One was at the corner of the heater, while the other was at the center of the faceplate, both on the forward faceplate surface. These stresses are shown as a function of the heat flux and faceplate thickness of 2.5 mm in Figure 6. Table 3 shows the heat flux for onset of yielding for several thicknesses and both plate materials. Thermal stresses greatly exceed pressure stresses at yielding.

Experimental Results

Power generation and heat flux

Electric power was supplied by a DC motor-generator set rated 3,000 A at 24 VDC. The heating apparatus reached power levels of more than 17 kW with currents above 2,000 A. The power generated was determined by measuring the current through and voltage drop across the thin-film heater. The voltage drop was measured using leads attached to the bus bars; the current was measured using a shunt. The uncertainties in both measurements are small.

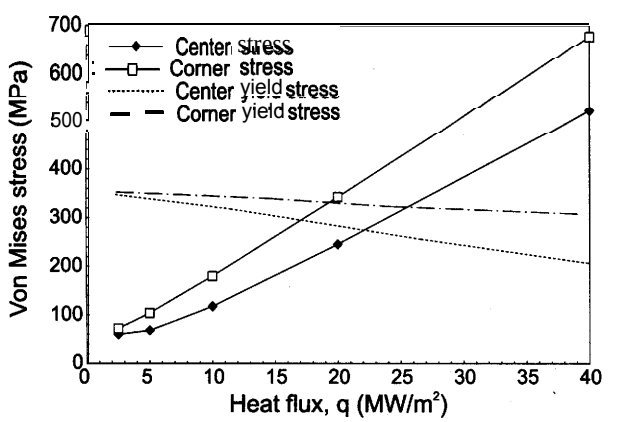

Figure 6. Stress vs. heat flux for a 2.5 mm Cl5715 faceplate.

Table 3. Heat Flux at Yielding (MW/m^2) as Determined by FEM Simulations.

Plate Thickness	Materials	
	Cl5715	TZM
2.5 mm	19 comer,	23 comer
3.0 mm	18 c o m e r	21 center
4.0 mm	17 center and comer	17 center

*Location of yielding as indicated.

Estimates of heat losses by radiation from the heater and conduction into the bus bars were made. As an upper bound, if the heated surface is assumed to behave as a black body, less than 0.3% of the total power generated is lost to the surrounding erivironment by radiation. At maximum power, conduction losses through the copper bus bars have been measured to be approximately 3% or less.

The applied heat flux q delivered by the heating element was calculated by dividing the electrical power dissipated by the active area of the heater film ($10.3\ cm^2$). This heat flux represents the cooling capacity of the modules; the measurement uncertainty at a 2σ level is less than 10%, accounting for uncertainty in electrical power and heater area. The flux on the liquid side of the faceplate decreases near the edges of the heated region owing to fin conduction in the faceplate; separate finite-element analyses (Dahbura and Younis, 1997) show that the liquid-side flux in the central 50% of the heated region is equal to that applied by the heater. On the outside edges of the heated region, the liquid-side flux is some 50% lower,

Heating data and thermal resistance

Temperature measurements were made over the heater film using 4 to 6 type K thermocouples cemented onto its surface. The heater surface temperature measurements were averaged and used to compute the average total temperature difference AT between the heater surface and the average bulk temperature of the water. Figure 7 shows the heat flux as a function of the average temperature difference between the liquid and heater surface for APS Data Sets A through G. The slope of these curves is the total thermal resistance from the heater surface to the flowing liquid. The vertical

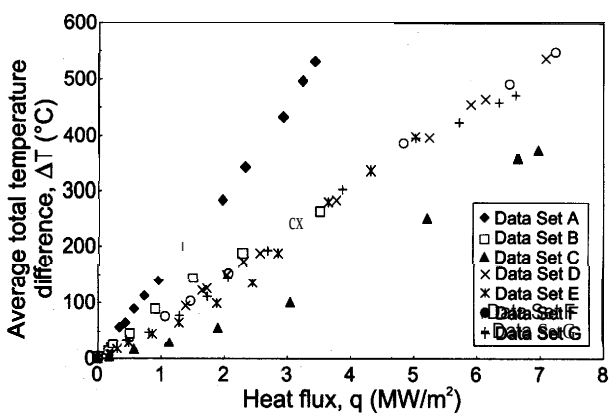

Figure 7. Average temperature difference between the bulk liquid and the APS heater film's upper surface.

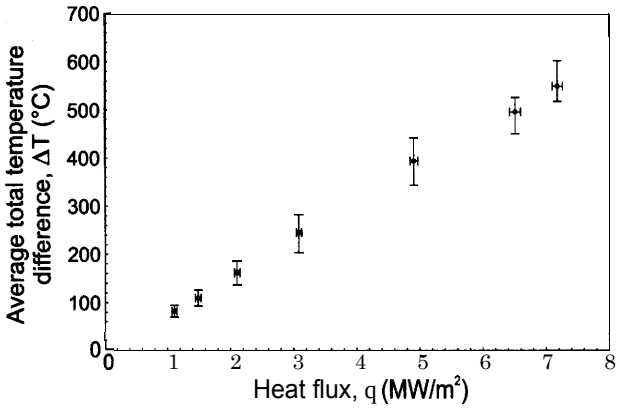

Figure 8. Average temperature difference between the bulk liquid and the heater film's upper surface for Data Set F.

error bars as in Figure 8 represent highest and lowest measured temperatures on the surface of an APS heater film. Figure 9 shows q vs. AT for nickel-chromium heaters produced by VPS or HVOF on alumina insulators produced by HVOF. These heaters, having better material properties, survived to higher fluxes than the APS heaters, and did so at lower temperatures. Fluxes of up to 17 MW/m^2 were reached before heater failure. (This highest flux approaches the yield limit of the faceplate involved.)

The graphs generally illustrate that the heat flux was linearly dependent upon the temperature difference, although some increase in the slope may occur due to the decreasing thermal conductivity of the ceramic layer with increasing temperature. This behavior is consistent with purely convective heat removal from the faceplate. Because most of the thermal resistance in the system results from the heater and insulator films, these graphs would not be expected to reveal nonlinearity in the $q-$ AT curve such as might follow the onset of boiling. However, measurements of the liquid-side temperature of the faceplate using thermocouples implanted in the faceplate show that the liquid-side temperature is below the saturation temperature at the largest flux obtained. These thermocouple measurements also provide an experimental value for the mean heat-transfer coefficient at our

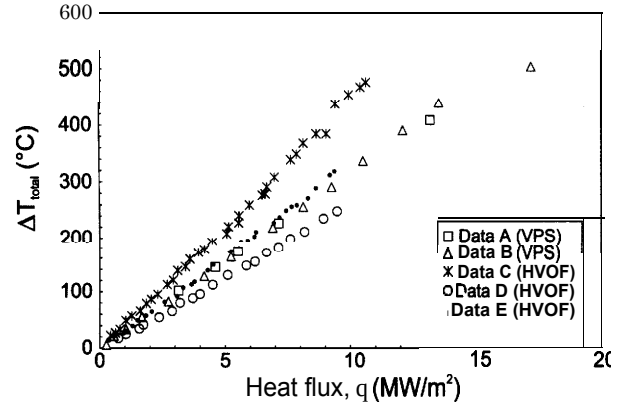

Figure 9. Difference between average surface temperature and coolant bulk temperature as a function of heat flux for HVOF/VPS heater films.

Table 4. Thermal Resistances for Various APS Heater/Faceplate Configuration! at AT ≈ 300°C

Data Set	R_{total} ($m^2 \cdot K/MW$)	R_{plate} ($m^2 \cdot K/MW$)	R_{films} ($m^2 \cdot K/MW$)
A	147 ± 24	8.57	133 ± 24
B	76 ± 21	8.57	62 ± 21
C	59 ± 15	8.57	45 ± 15
D	77 ± 3	27.6	44 ± 3
E	78 ± 21	20.0	53 ± 21
F	80 ± 12	20.0	55 ± 12
G	78 ± 11	20.0	53 ± 11

operating' condition of 2.1×10^5 $W/m^2 \cdot K \pm 20\%$ (at a 2σ level). Ongoing work in our lab is aimed at refining these measurements.

The thermal resistance of the APS films is shown in Table 4. Thermal resistances were calculated on a one-dimensional basis and represent conditions within the central portion of the heated region The thermal resistance of the films was separated from the total resistance by subtracting the thermal resistance of the boundary layer and the faceplate

$$R_{films} = R_{total} - R_{plate} - R_{bl} = \frac{AT}{q} - \frac{t_p}{k_p} - \frac{1}{h} \qquad (5)$$

As calculated, the film resistance includes the conduction and interfacial resistances associated with the heater and ceramic layers. Due to the large convective heat-transfer coefficient, the uncertainty in the boundary layer thermal resistance has only a minor impact on the value calculated for the thermal resistance of the films.

For all experiments reported, the heating elements fractured at fluxes slightly beyond the highest values reported. Fracture resulted from stresses in the heater films that caused the heater film to crack and delaminate from the faceplate. Heating element failure was not related to the cooling capabilities of the module.

Numerical Procedure for Flow Analysis

The flow and temperatures were simulated numerically and the average temperatures on the heater surface were compared with measured temperatures. The renormalization group (RNG) $k-\epsilon$ turbulence model was used in this study.

The cooling module contains 3-D turbulent flow (the Reynolds number at the exit of the nozzle is 128,600 based on a bulk temperature of 20°C) with high heat flux on the faceplate rear. In these calculations, an assumption of 2-D flow is made because of the approximate axisymmetry of the central jets in the cooling module. This assumption was found to be valid by comparison to a 3-D simulation for one of the cases.

Incompressible, steady-state, turbulent flows can be expressed in a canonical form (Patankar, 1980). Elliptic differential equations govern the axisymmetric flow in the cooling module.

$$\frac{\partial}{\partial x}(\rho u \Phi) + \frac{1}{r}\frac{\partial}{\partial r}(\rho r v \Phi) - \frac{\partial}{\partial x}\left(\Gamma_{eff}\frac{\partial \Phi}{\partial x}\right) - \frac{1}{r}\frac{\partial}{\partial r}\left(r\Gamma_{eff}\frac{\partial \Phi}{\partial r}\right) = S_\Phi \qquad (6)$$

Table 5. Expressions for the Independent Variables in Eq. 6

Variable	Φ	Source term, S_Φ	Γ_{eff}
Continuity	l	0	0
Axial momentum	u	$\frac{\partial}{\partial x}\left(\Gamma_{eff}\frac{\partial u}{\partial x}\right)+\frac{1}{r}\frac{\partial}{\partial r}\left(\Gamma_{eff}r\frac{\partial v}{\partial x}\right)-\frac{\partial P}{\partial x}$	μ_{eff}
Radial momentum	v	$\frac{\partial}{\partial x}\left(\Gamma_{eff}\frac{\partial u}{\partial r}\right)+\frac{1}{r}\frac{\partial}{\partial r}\left(\Gamma_{eff}r\frac{\partial v}{\partial r}\right)-\frac{\partial P}{\partial r}-2\Gamma_{\text{eff}}\frac{v}{r^2}$	μ_{eff}
Energy	h	$\frac{\mu}{Pr}+\frac{\mu_t}{\sigma_t}$	F_{11}
Turbulent Kinetic Energy (RNG)	k	$\frac{\mu_l}{\sigma_k}$	$\mu_t S^2-\rho\epsilon$
Dissipation rate of turbulence energy (RNG)	ϵ	$\frac{\mu_t}{\sigma_e}$	$C_1\frac{\epsilon}{k}\mu_t S^2-C_2\rho\frac{\epsilon}{k}-R$

where

$\mu_{\text{eff}}=C_\mu \rho\frac{k^2}{\epsilon}$, $S^2=2S_{ij}S_{ij}$ (the modulus of the rate of strain tensor)

$R=\frac{0.0845\eta^3(1-\eta/\eta_0)}{1+0.01273}\rho\frac{\epsilon^2}{k}$, $\eta=(Sk)/\epsilon$, $\eta_o=4.38$, $Pr=C_p\frac{\mu}{k}$

F_{11} = viscous heating term; h = total specific enthalpy

Constants $C_1=1.42, C_2=1.68, C_\mu=0.09, \sigma_k=1.0, \sigma_\epsilon=1.3$

where x is the coordinate in the main flow direction, r is the radial coordinate, p is the fluid density, and u and v are velocity components in the x- and r-directions, respectively. S_Φ is the source term and Γ_{eff} is the effective viscosity or diffusivity for the different variables Φ as given in Table 5. The standard procedure for converting this equation into a finite difference equation is to integrate it over a control volume and evaluate the respective fluid properties at the control volume boundaries.

In this study, the RNG $k-\epsilon$ turbulence model (Yakhot and Orszag, 1986) is used. The RNG-based $k-\epsilon$ turbulence model follows the two-equation turbulence modeling framework and uses dynamic scaling and invariance together with iterated perturbation methods, A study performed by Orszag et al. (1993) indicates that the RNG $k-\epsilon$ turbulence model is more accurate than the standard $k-\epsilon$ turbulence model, particularly for recirculating flows (Freitas, 1995).

The numerical techniques described thus far are available from several commercial computational fluid dynamics software packages (e.g., Fluent, 1997). The effective viscosity is defined by the relation

$$\mu_{\text{eff}}=\mu+\mu_t \tag{7}$$

where μ is the molecular viscosity and μ_t is the turbulent viscosity deduced by employing a turbulence model.

In the near-wall region of the thin boundary layer that is generated due to impinging jets, non-equilibrium wall functions are used to improve the quality of prediction. The non-equilibrium wall functions include pressure gradient effects in Launder and Spalding's (1974) log-law for mean velocity, and adoption of the two-layer-based concept that computes turbulent kinetic energy in the wall-neighboring cells. The log-law for mean velocity sensitized to pressure gradients is

$$\frac{\bar{U}C_\mu^{1/4}k^{1/2}}{\tau_w/\rho}=\frac{1}{\kappa}\ln\left(9.81\frac{\rho C_\mu^{1/4}k^{1/2}y}{\mu}\right) \tag{8}$$

where

$$\bar{U}=U-\frac{1}{2}\frac{dp}{dx}\left[\frac{y_v}{\rho k^o k^{1/2}}\ln\left(\frac{y}{y_v}\right)+\frac{y-y_v}{\rho k^o k^{1/2}}+\frac{y_v^2}{\mu}\right] \tag{9}$$

κ is von Karman's constant, y is the distance from the wall, τ_w is the shear stress at the wall, y_v is the physical viscous sublayer thickness, and is computed from

$$y_\nu\equiv\frac{\mu y_v^o}{\rho C_\mu^{1/4}k_p^{1/2}} \tag{10}$$

where $y_v^o=11.225$. The following formulations for turbulence quantities are made:

$$\tau_t=\begin{cases}0 & y<y_v\\ \tau_w & y>y_v\end{cases} \tag{11}$$

$$k=\begin{cases}\left(\frac{y}{y_v}\right)^2\kappa_p & Y<y_v\\ k_p & Y>Y''\end{cases} \tag{12}$$

$$\epsilon=\begin{cases}\frac{2\nu k}{y^2} & y<y_v\\ \frac{k^{3/2}}{C_l y} & y>y_v\end{cases} \tag{13}$$

where $C_l=kC_\mu^{-3/4}$ and y_v is the dimensional thickness of the viscous sublayer defined in Eq. 10.

Numerical Results for Flow and Heat Transfer

The simulation is axisymmetric, and the secondary stagnation zone at the outside of the flow domain is modeled as a circle of 5 mm (0.197 in.) radius having a symmetry boundary condition (zero gradients). The detailed model geometry can be found in Lienhard et al. (1997, Sect. C). The computational grid is 225×40 (axial and radial-directions, respectively) for the flow domain. The grid is uniform for grid lines covering the inlet nozzle. Outside this uniform region the grid is stretched with a factor 1.1 in the radial direction. The size of the near wall grids has been chosen such that y_v^o is close to 11.3. The solution's dependency on the grid has been tested with successively finer grid size until the solution became grid independent. The heat flux, q, is applied to the dry side of the faceplate (made of either alloy Cl5715 or TZM). The nozzle outlet to faceplate separation was varied from 1.79 jet diameters to 7 jet diameters behind the faceplate. The flow velocity at the nozzle outlet was varied, as was the heat flux applied to the outer surface of the DS copper (C15715) plate or molybdenum alloy (TZM) plate. A 2-mm (0.079-in.) thick plate was used for all the simulations.

The nozzle is made of steel with a thickness of 1.785 mm (0.0703 in.) Water was used as a jet fluid and thermal conductivities of conducting materials were input as a function of temperature up to 725°C.

Figure 10 shows the radial pressure distribution on the liquid-side of the copper plate, the faceplate rear, at jet inlet velocities of 20, 30 and 46.47 m/s. The pressure results are very consistent with our expectations. The highest-pressure region in all three cases was at the stagnation points, with the pressure dropping to a minimum at $r/d = 1.2$ between the primary and secondary stagnation zones. When the nozzle-to-target separation is reduced, the minimum pressure is reduced. At the secondary stagnation zone, the pressure rises slightly again due to conservation of momentum,

A primary concern for jet array impingement cooling at these high fluxes is the possibility of boiling in the low-pressure regions between the primary and the secondary stagnation zones. Even though boiling tends to increase the convective heat transfer locally, it interferes with the flow downstream of the jet and can eventually lead to burnout. If the pressure is predicted to be lower than saturation, a back pressure is applied in the experiments to raise pressure above the saturation value to suppress boiling. In Figure 10, a back pressure of 551 kPa has been assumed; the minimum pressure is above saturation and no boiling is expected.

Figure 11 shows the radial component of liquid velocity as a function of radius for three different nozzle inlet velocities. As shown, the radial velocities are zero at the stagnation point and accelerate in the mid-radial locations where the static pressures shown in Figure 10 are minimum.

Figure 12 shows axial velocity contours downstream of the nozzle. As shown in Figure 12, the axial velocity is zero when the liquid reaches the stagnation point. At the secondary stagnation region, the flow exits along the symmetry line showing negative values.

Figure 13 shows the static pressure distribution. The static pressure depicted in Figure 13 shows higher pressure in the stagnation points which can be explained by the approximate conservation of the total pressure.

Figure 14 shows results of variations of the nozzle-to-diameter (z/d) ratio on Nusselt number using two different Reynolds numbers 128,600 and 82,900, and a heat flux of 7.025 MW/m^2 (Re $= u_j d/\nu$ for $\nu = 10^{-6}$ m^2(s). These results are

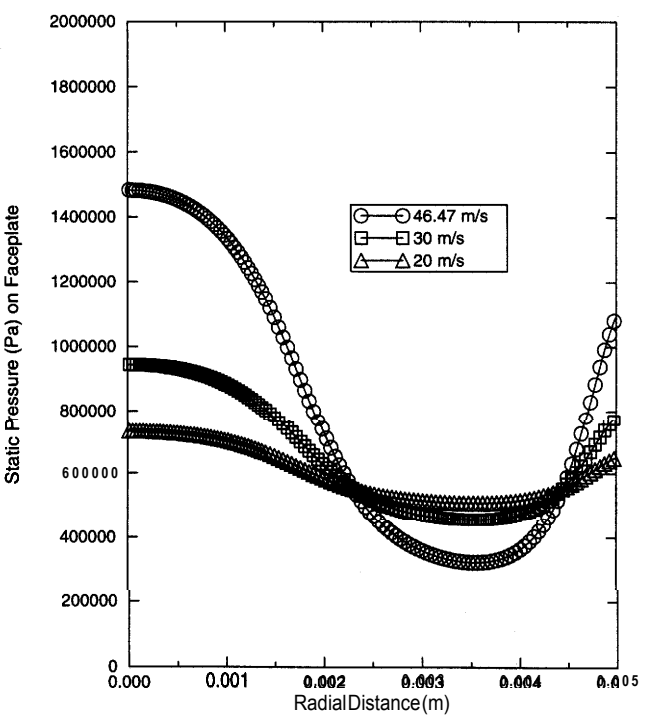

Figure 10. Calculated variation of pressure vs. radial distance from stagnation point for three velocities at z/d= 1.79, and 9= 7.025 MW/m².

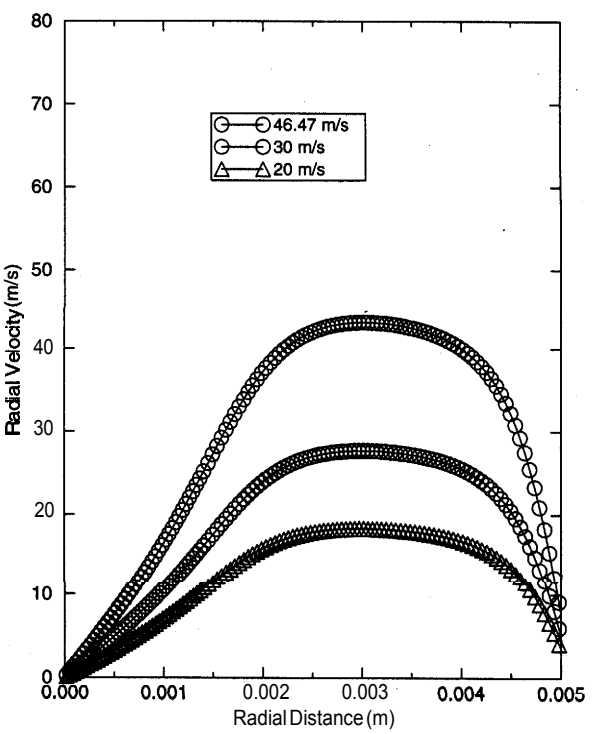

Figure 11. Radial liquid velocity outside boundary layer vs. radial distance for three velocities at z/d = 1.79 and 9= 7.025 MW/m².

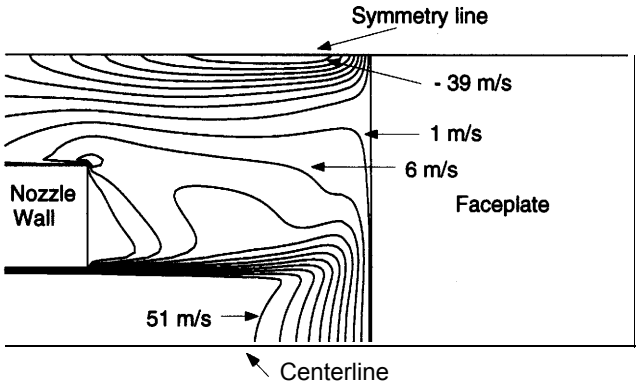

Figure 12. Calculated axial velocity contours at u = 46.47 m/s, z/d = 1.79, and q = 7.025 MW/m².

compared with those of Sun et al. (1993). As shown in Figure 14, the maximum heat transfer occurs at $z/d = 6$ for the Reynolds number of 128,600 (46.47 m/s velocity) and 82,900 (30 m/s velocity). For lower Reynolds numbers and heat flux data in the literature (Sun et al., 1993), the maximum heat transfer occurs at $z/d = 5$.

Table 6 shows the comparison of measured and calculated temperatures at a 46.47 m/s velocity. The local heat-transfer coefficients on the liquid side of the faceplate were calculated using the RNG turbulence model. As shown in the table, the average heat-transfer coefficients are approximately 210,000 MW/m²·K. The film thermal resistance used in the calculations has been estimated at each temperature from the measurements described above. The measured average heater-surface temperatures are compared with the calculations and agree to within 5%. As was previously noted, the local temperatures in the heater films may vary by more than 5%, particularly if the heater film is too thin.

Conclusions

A liquid jet array cooling module has been developed and tested at heat fluxes of up to 17 MW/m². Module performance was limited only by the failure of the heating elements. Boiling is expected only for fluxes well above 20 MW/m². Yielding of the faceplate is expected for fluxes of 17 to 23 MW/m² depending on the plate thickness.

Numerical calculations were performed to find the detailed flow characteristics and temperatures. Measured faceplate front temperatures agreed well with calculated ones. The heat transfer in the cooling module is dominated by thermal resistances to the insulating film between the test heater and the faceplate. The heat-transfer coefficients are calculated using the RNG turbulence model. The averaged heat-transfer coefficients using the RNG $k-\epsilon$ model are 210,000 MW/m²·K at a Reynolds number of 128,600.

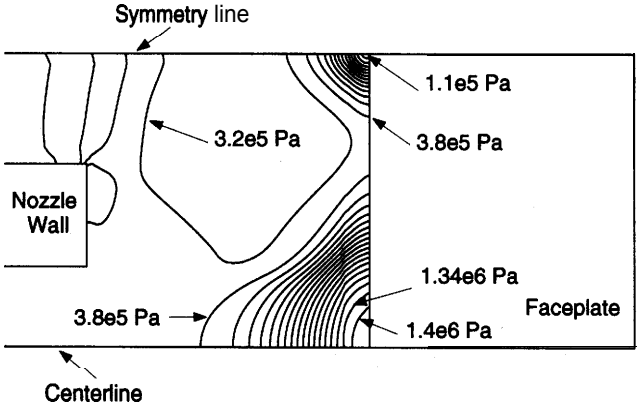

Figure 13. Calculated static pressure contours at u = 46.47 m/s, z/d = 1.79, and 9 = 7.025 MW/m².

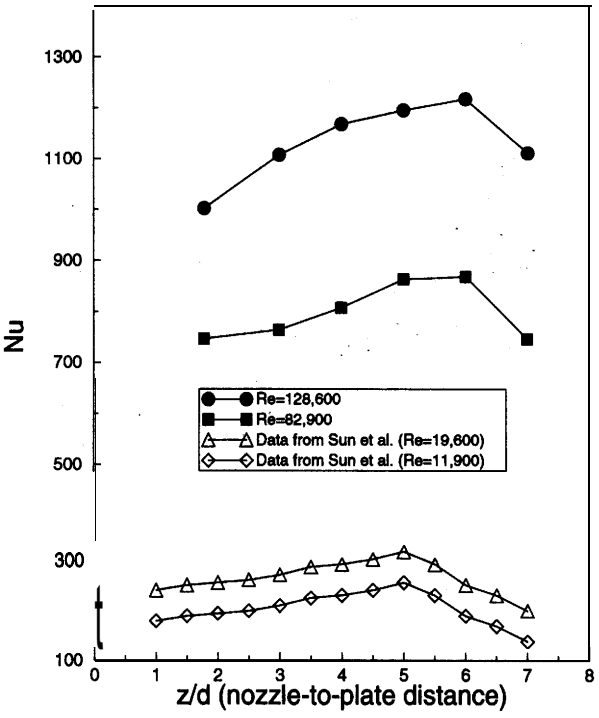

Figure 14. Variation of the stagnation Nusselt number as a function of nozzle-to-plate distance.

Acknowledgment

This work was performed under the auspices of the U.S. Dept. of Energy, Laboratory Directed Research and Development Program and INEEL University Research Consortium, under the DOE Operations Office Contract No. DE-AC0794ID13223.

Table 6. Comparison of Data (Set A in Table 4) to Calculated Heater Surface Temperatures and Heat-Transfer Coefficients from the Renormalization-Group Model (RNG)

Heat Flux	$R_{th,\ films}$	Meas. Temp.	Calc. Temp.	Calc. Heat Transf. Coeff.
(MW/m²)	(m²·K/MW)	(°C)	(°C)	(W/m²K)
3.153	44.39	277	266	210,963
3.787	44.64	327	317	210,966
4.329	45.35	372	358	210,962
5.281	44.98	440	426	210,962
5.861	46.47	500	475	212,414
6.082	45.46	511	491	210,960
7.025	44.92	581	5 5 8	216,393

Literature Cited

Cooper, D., D. C. Jackson, B. E. Launder, and G. X. Liao, "Impinging Jet Studies for Turbulence Model Assessment: I. Flow-Field Experiments," *Int. J. Heat Mass Transf.*, **36**, 10, 2675 (1993).

Craft, T. J., L. J. W. Graham, and B. E. Launder, "Impinging Jet Studies for Turbulence Model Assessment: II. An Examination of the Performance of Four Turbulence Models," *Int. J. Heat Mass Transf.*, **36**, 10, 2685 (1993).

COSMOS/M Version 1.75, Los Angeles, CA, Structure Research and Analysis Corporation (1995).

Dahbura, R. S., and H. F. Younis, "Thermal and Mechanical Development of Extremely High Heat Flux Cooling Modules Based on Jet Array Technology," SM Thesis, Dept. of Mechanical Engineering, Massachusetts Institute of Technology, Cambridge (1997).

FLUENT, Version 4.4.4, Lebanon, NH, Fluent, Inc. (1997).

Freitas, C. J., "Perspective:Selected Benchmarks from Commercial CFD Codes," *J. Fluid Eng.*, 117, 209 (1995).

Katto, Y., and M. Shimizu, "Upper Limit of CHF in the Saturated Forced Convection Boiling on a Heated Disk with a Small Impinging Jet," *J. Heat Transf*, **101, 265** (1979).

Launder, B. E., and D. B. Spalding, "The Numerical Computation of Turbulence Flows," *Comput. Methods in Appl. Mechanics and Eng.*, **3, 269** (1974).

Lienhard V, J. H., "Liquid Jet Impingement," *Annual Review of Heat Transfer*, C. L. Tien, ed., Vol. 6, Begell House, New York, 199 (1995).

Lienhard V, J. H., R. S. Dahbura, and H. F. Younis, "Thermal and Mechanical Development of Extremely High Heat Flux Cooling Modules Based On Jet Array Technology," Annual Report to the INEEL University Research Consortium, Dept. of Mechanical Engineering, Massachusetts Institute of Technology, Cambridge (1997).

Lienhard V, J. H., R. S. Dahbura, H. F. Younis, and C. H. Oh, "Large Area Jet-Array Cooling Modules for High Heat Fluxes," *High Heat Flux Engineering III*, Proc. SPIE, Vol. 2855, SPIE, Bellingham, WA, 66 (1996).

Lienhard V, J. H., H. F. Younis, R. S. Dahbura, and C. H. Oh, "Experiments on Jet-Array Cooling Modules for High Heat Flux Removal," *High Heat Flux and Synchrotron Radiation Beamlines*, Proc. SPIE, Vol. 3151, SPIE, Bellingham, WA, 6 (1997).

Lienhard V, J. H., and D. S. Napolitano, "Yield Limits of Plates at Extremely High Heat Flux," *J. Heat Transf, 120, 253* (1998).

Liu, X., and J. H. Lienhard V, "Extremely High Heat Fluxes Beneath Impinging Liquid Jets," *J. Heat Transf*, **115, 472** (1993).

Liu, X., L. A. Gabour, and J. H. Lienhard V, "Stagnation-Point Heat Transfer During Impingement of Laminar Liquid Jets: Analysis Including Surface Tension," *J. Heat Transf.*, **115, 99** (1993).

Liu, X, J. H. Lienhard V, and J. S. Lombara, "Convective Heat Transfer by Impingement of Circular Liquid Jets," *J. Heat Transf, 113, 571* (1991).

Ma, C.-F., and A. E. Bergles, "Convective Heat Transfer on a Small Vertical Heated Surface in an Impinging Circular Liquid Jet," *Heat Transfer Science and Technology*, B.X. Wang, ed., Hemisphere, New York, p. 193 (1988).

Meyer, K. E., "Experimental and Numerical Investigation of Turbulent Flow and Heat Transfer in Staggered Tube Bundles," PhD Thesis, Dept. of Fluid Mehanics, Technical Univ. of Denmark, (Jan., 1994).

Michels, D., J. Hadeler, and J. H. Lienhard V, "High Heat Flux Resistance Heaters from VPS and HVOF Thermal Spraying," *Expt. Heat Transf., in* press (1998).

Orszag, S. A., V. Yakhot, W. S. Flannery, and F. Boysan, "Renormalization Group and Turbulence Simulations," *Near-Wall Turbulence Flows*, R.M.C. So, C.G. Speziale, and B.E. Launder,, eds., Elsevier Science, New York (1993).

Owsenek, B. L., T. Cziesla, N. K. Mitra, and G. Biswas, "Numerical Investigation of Heat Transfer in Impinging Axial and Radial Jets with Superimposed Swirl," *Int. J. Heat Mass Transf , 40*, 1, 141 (1997).

Pan, Y., and B. W. Webb, "Heat Transfer Characteristics of Arrays of Free-Surface Liquid Jets," *J. Heat Transf., 117, 4, 878* (1995).

Patanka, S. V., *Numerical Heat Transfer and Fluid Flow*, Hemisphere, Washington, DC (1980).

Sampath, S., and H. Herman, "Rapid Solidification and Microstructure Development During Plasma Spray Deposition," *J. Thermal Spray Technol., 5, 445* (1996).

Stevens, J., and B. W. Webb, "Local Heat Transfer Coefficients Under an Axisymmetric, Single-Phase Liquid Jet," *J. Heat Transf , 113, 71* (1991).

Sun, H., C. F. Ma, and W. Nakayama, "Local Characteristics of Convective Heat Transfer from Simulated Microelectric Chips to Impinging Submerged Round Water Jets," J. *Electron, Packag.*, **115**, 71 (1993).

Viskanta, R., "Heat Transfer to Impinging Isothermal Gas and Flame Jets," *Thermal Fluid Sci.*, 6, 111 (1993).

Yakhot, V., and S. A. Orszag, "Renormalization Group Analysis of Turbulence: I. Basic Theory," *J. Sci. Comput.*, **1**, 1, 3 (1986).

Younis, H. F., R. S. Dahbura, and J. H. Lienhard V, "Thin Film Resistance Heaters for High Heat Flux Jet-Array Cooling Experiments," *Proc. ASME Heat Transfer Div.*, ASME HTD-Vol. 353, 127 (1997).

Manuscript received Sept. 19, 1997, and revision received Jan. 30, 1998.